Icarus 273 (2016) 205–213

Contents lists available at ScienceDirect

Icarus

journal homepage: www.elsevier.com/locate/icarus

The temperatures of Giordano Bruno crater observed by the Diviner Lunar Radiometer Experiment: Application of an effective field of view model for a point-based data set

J.-P. Williams[a,*], E. Sefton-Nash[b], D.A. Paige[a,1]

[a] Dept. Earth, Planetary and Space Sciences, University of California, Los Angeles, CA 90095, USA
[b] Department of Earth and Planetary Sciences, Birkbeck, University of London, Malet Street, London WC1E 7HX, UK

ARTICLE INFO

Article history:
Received 29 June 2015
Revised 30 September 2015
Accepted 29 October 2015
Available online 14 November 2015

Keywords:
Moon
Moon, surface
Regoliths
Cratering
Infrared observations

ABSTRACT

Point based planetary datasets are typically stored as discrete records that represent an infinitesimal location on the target body. Instrumental effects and spacecraft motion during integration time can cause single points to inadequately represent the total area on the target that contributes to an observation. Production of mapped data products from these data for scientific analysis proceeds by binning points onto rectangular grids. Empty bins occur where data coverage is insufficient relative to grid resolution, a common problem at high latitudes in cylindrical projections, and remedial interpolation can lead to high uncertainty areas and artifacts in maps.

To address such issues and make better use of available data, we present a method to calculate the ground-projected effective field of view (EFOV) for point-based datasets, using knowledge of instrumental characteristics and observation geometry. We apply this approach to data from the Lunar Reconnaissance Orbiter (LRO) Diviner Lunar Radiometer Experiment, a visible to far-infrared multispectral radiometer which acquires radiometric measurements of reflected visible and emitted infrared radiation of the Moon in 9 spectral channels between 0.35 and 400 μm. Analysis of gridded radiance from crater Giordano Bruno, a 22 km diameter rayed crater, is used to demonstrate our gridding procedure. Diviner data, with such processing, reveals details of the surface that are seen in the high-resolution LRO Camera NAC images. Brightness temperatures and anisothermality observed in Diviner's IR channels show the thermophysical properties of the crater ejecta to be very heterogeneous indicative of minimal mechanical disruption by micrometeoroid impacts consistent with a very young (<10 Ma) formation age as the lunar surface becomes rapidly homogenized over time. This heterogeneity has implications for crater-count studies as regions of high anisothermality are characterized by large blocks of material and lower crater densities.

1. Introduction

The Diviner Lunar Radiometer Experiment (Paige et al., 2010a) is one of seven instruments aboard NASA's Lunar Reconnaissance Orbiter (LRO) (Chin et al., 2007; Tooley et al., 2010; Vondrak et al., 2010). Diviner began operating July 5, 2009, mapping the Moon on a nearly continuous basis, acquiring calibrated radiometric measurements of reflected visible, and emitted infrared radiation of the Moon in 9 spectral channels covering a wavelength range of 0.3–400 μm. Each Diviner channel is comprised of a 21-element thermopile detector array and spectral filter. The instrument nominally points in the nadir direction operating as a multi-spectral pushbroom mapper. Observations are acquired continuously with a 0.128 s signal integration period, providing a swath width of 3.4 km and a nominal instantaneous field of view (IFOV) of 320 m in-track and 160 m cross-track for each detector at an orbital altitude of 50 km.

The Diviner Commissioning and Primary Mapping dataset, covering July 5, 2009 to September 15, 2012, have been gridded into global brightness temperature maps referred to as Diviner Global Data Records (GDR), which have been archived at the NASA Planetary Geosciences Node (LRO-L-DLRE-5-GDR-V1.0) (Paige et al., 2011). These gridded data products were derived directly from the Reduced Data Records (RDR) products: level 1 calibrated radiance observations (Sullivan et al., 2013). Diviner GDR data products are

* Corresponding author. Fax: +1 310 825 2279.
E-mail addresses: jpierre@mars.ucla.edu (J.-P. Williams), e.sefton-nash@uclmail.net (E. Sefton-Nash), dap@moon.ucla.edu (D.A. Paige).
[1] Fax: +1 310 825 2279.

http://dx.doi.org/10.1016/j.icarus.2015.10.034
0019-1035/

not interpolated and include data gaps in grid cells where no observations were acquired.

The data gridding approach described in this paper was developed and used for the creation of all archived Diviner GDR products (Paige et al., 2011) and is routinely employed when gridding Diviner data. We therefore use Diviner as an example to illustrate our approach, though our procedure in this paper is not necessarily Diviner specific. We then present analysis of Diviner data from two orbits tracks crossing the crater Giordano Bruno showing how the thermal response of the surface material within and around the crater to solar forcing reveals a complex, and heterogeneous mixture of thermophysical properties, consistent with a very young crater that has experienced minimal processing by micrometeoroid bombardment.

2. Calculating the effective field-of-view (EFOV)

For an instrument operating in a pushbroom configuration like Diviner, the effective FOV in the in-track direction is broadened by two effects: (i) spacecraft motion relative to the target body during the sample integration time $b(t)$ and (ii) the exponential detector thermal response time $d(t)$. These effects result in elongation of the FOV in the in-track direction, and along with the instrument's instantaneous field of view (IFOV) $f(t)$, define the total contribution to an observation. Knowing the shape of these functions, for each observation we may construct a 2D probability distribution in the focal plane of the detector – equal to a convolution of the component functions evaluated over the integration time: $[(b * d) * f](t)$. This EFOV describes the likelihood of quanta e.g., photons, originating from a given location within an observation's ground projected footprint.

In order to produce mapped data products, the probability function must be discretized into points so that they may be projected onto the surface of the target body (assuming there is knowledge of the observation geometry), and subsequently binned onto regular grids. This is accomplished by populating the EFOV with a Monte Carlo distribution comprising n points, where the weight of each point $w = 1/n$ observations. The term n must be sufficient to adequately resolve the EFOV with the modeled EFOV tending to the actual EFOV with increasing n.

The instantaneous field of view for each Diviner detector was measured in the laboratory prior to integration with LRO (see Paige et al. (2010a) for details). The average IFOV of all 21 detectors for each channel are shown in Fig. 1 with measured step sizes of 0.39 mrad and 0.19 mrad for in-track and cross-track scans, respectively. Shoulders with a magnitude ~5–10% of the central peak in the cross-track IFOVs are due to thermal crosstalk between adjacent detectors. Channels 2 and 6 are narrow in the in-track IFOVs due to reduced apertures over these spectral filters. The three longest wavelength channels (7–9) have the broadest fields of view due to the mesh filters employed for these channels (Paige et al., 2010a).

Each detector has a thermal response time associated with it (i.e. each detector has a memory of an observation that decays exponentially with time). Table 1 shows the response time, $t_\circ$, for the individual Diviner channels. The exponential function representing the detector response time is $\exp(\alpha/x_\circ)$, where α is the angular distance in radians from the center of the observation (assumed to be nadir pointing in this discussion) and $x_\circ = \tan^{-1}(v_{sc}t_\circ/z_{sc})$ is a decay constant related to the detector response time, the spacecraft velocity v_{sc}, and altitude z_{sc} at the mid-point of the observation. Spacecraft motion during the 128 ms sample integration time results in additional smearing in the in-track direction represented by a triangular function (Fig. 2). The effective in-track FOV is then the convolution of the triangular function with the in-track IFOV and the exponential function representing the detector response

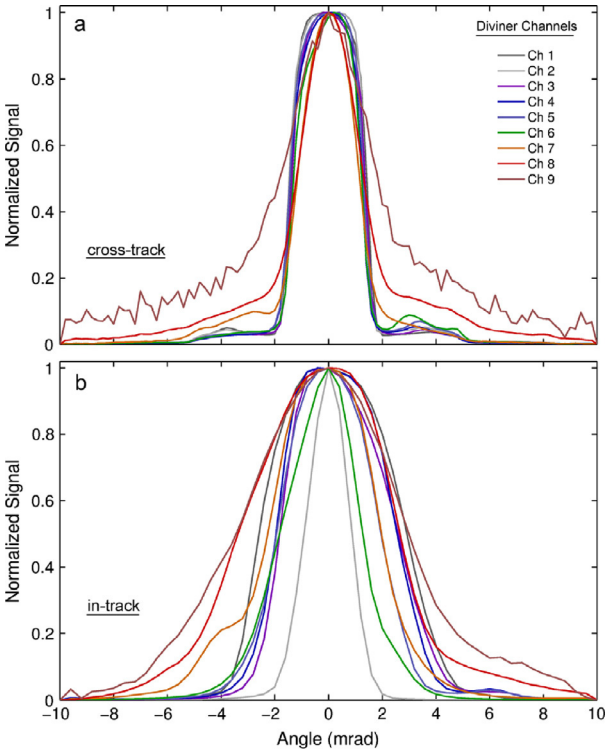

Fig. 1. (a) Cross-track and (b) in-track instantaneous fields of view of Diviner channels.

Table 1
Diviner exponential detector thermal response times.

Channel	Passband (μm)	Response time, $t_\circ$ (ms)
1	0.35–2.8	110
2	0.35–2.8	110
3	7.55–8.05	119
4	8.10–8.40	123
5	8.38–8.68	123
6	13–23	117
7	25–41	127
8	50–100	131
9	100–400	147

time. Fig. 2 shows the Diviner channel 4 IFOVs, the two functions representing integration time and detector response time broadening, and the EFOV resulting from the convolution of the other three functions assuming the LRO nominal mapping orbit configuration: near-circular orbit at an altitude ~50 km with a ground speed ~1.66 km s^{-1}. All functions are normalized to a value of one. No broadening occurs in the cross-track direction. The resulting two-dimensional EFOV is ellipsoidal with elongation in the in-track direction. The resulting shape of the EFOV will depend on altitude and ground speed and therefore will differ with changing orbital parameters.

3. Gridding data

In determining the effective surface footprint of the detectors, the orientation of the detectors must first be determined. Fig. 3 shows the basic viewing geometry of the array of Diviner detectors. To determine their orientation relative to north, we define a plane determined by the vector from the center of the Moon to the latitude and longitude of the point observation on the surface, **s**, and the vector defining the lunar spin axis in the north direction **N**. The orientation of the detectors is defined by a vector **d**, aligned with the detector array and projected from the lunar center to the

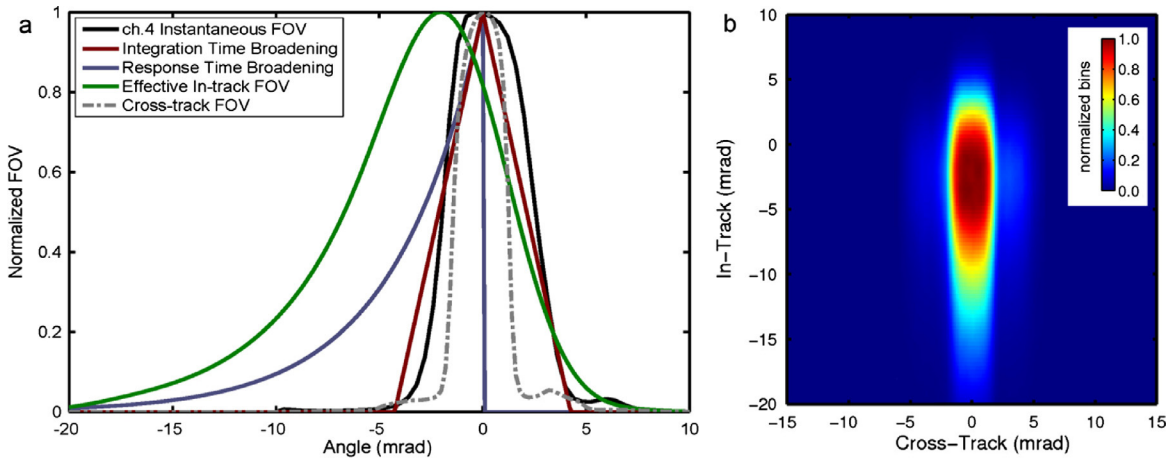

Fig. 2. (a) Diviner channel 4 cross-track IFOV (gray dot-dash) and in-track IFOV (black) plotted along with in-track broadening functions due to sample integration time (red) and detector thermal response time (blue) for a spacecraft altitude of 50 km and velocity 1.66 km s^{-1}. The in-track effective FOV (green) is the convolution of the three in-track functions. Spacecraft motion is from left to right. (b) The two-dimensional probability distribution of the resulting effective Diviner surface footprint represented as a normalized 100 × 100 bin two-dimensional histogram using 1×10^6 points. The axes correspond to horizontal distances ~750 m for a spacecraft altitude of 50 km. (For interpretation of the references to color in this figure legend, the reader is referred to the web version of this article.)

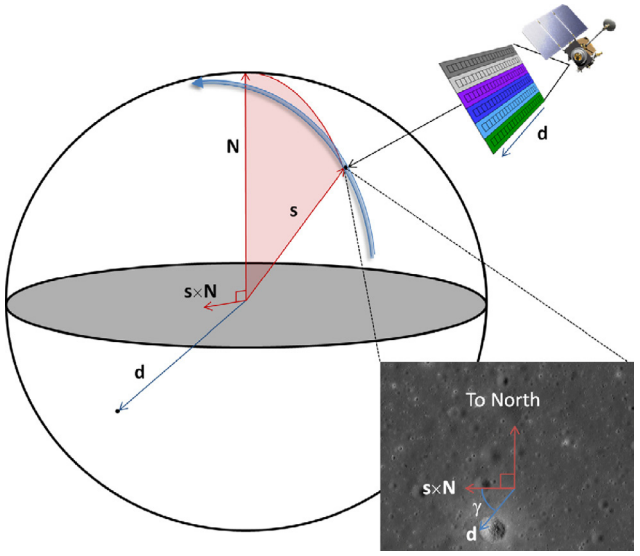

Fig. 3. Spacecraft viewing geometry showing the alignment of the Diviner detectors relative to the vectors described in the text. Vectors have the lunar center as their origin. Vector **d** defines the detector array orientation in terms of the longitude and latitude at the lunar surface intersected by the vector from the origin. Vector **s** defines the surface observation and **N** the lunar spin axis in the north direction. The angle, γ, is the rotation of the detectors relative to north. The inset depicting the lunar surface shows the vectors projected onto the surface at the observation point.

lunar surface. The angle γ between the plane normal (**s** × **N**) and **d** is then derived from their dot product and provides the angular rotation of the detectors from north.

Diviner is in a polar orbit, however the orbit is generally several degrees off the pole and therefore there is generally an angular offset from north. Diviner is a pushbroom radiometer and nominally operates in a nadir-pointing mapping mode with the detectors aligned perpendicular to the ground track. The orientation of the detectors also reverses when the spacecraft performs a 180° yaw maneuver, which is done every six months to keep the Sun on the same side (Tooley et al., 2010).

The EFOV, in the quasi-circular mapping orbit at an average altitude of ~50 km, results in a ground-projected footprint of ~500 × 100 m in the in-track and cross-track directions, respectively (Fig. 2). Though a measurement is represented by a single location on the surface, the total radiance that contributes to a measurement derives from a finite surface area described by the two-dimensional EFOV projected onto the surface. Binning the data onto a latitude/longitude grid can result in aliasing at high latitudes where the areal extent of the bins in longitude become increasingly smaller toward the pole. An example of this is shown in Fig. 4a where a portion of Diviner level 1 RDR data (calibrated radiances) has been binned and mapped in an equidistant cylindrical projection at a resolution of 128 pixels per degree showing a swath of data from an individual orbit. This resolution is similar to the native resolution of Diviner at the equator. At higher latitudes, above ~60° depending on spacecraft altitude (latitudes 65.5–66.5° shown in the example), grid spacing becomes narrow enough in longitude that not all bins within the interior of the orbit track are populated. However the areas represented by these unpopulated bins, contribute to the measurements being gridded. At an altitude of 50 km, the surface footprints of the detectors across the array overlap in the cross-track direction as do consecutive observations in the in-track direction.

Other issues can arise when comparing different spectral channels, which has been done for several of Diviner's higher level data products (levels 3 and 4). For example, Diviner channels 3–5, which are centered around an emission peak at a wavelength of ~8 μm, are used to identify the bulk silicate mineralogy of the surface (Greenhagen et al., 2010; Glotch et al., 2010, 2011; Song et al., 2013). Anisothermality in nighttime observations in Diviner channels 6–8 has been used to map rock abundance and regolith fines temperature (Bandfield et al., 2011) and differencing brightness temperatures at morning and afternoon local times from Diviner channels 4 or 6 with channel 7 have been used to characterize surface roughness (Bandfield et al., 2015). The footprints of the detectors of the individual channels in general will not be identically aligned. This misalignment can be apparent when comparing individual Diviner channels when sharp thermal or compositional contrasts are encountered on the lunar surface. Artifacts can then result in datasets derived from multiple Diviner channels.

Issues such as these are resolved by modeling the ground projected footprint of each observation using the Monte Carlo method prior to binning the data. The two-dimensional EFOV is employed as a probability distribution of the radiance from the surface contributing to the observation (Fig. 2). The EFOV is populated with *n* points and projected onto the surface of the target body (Fig. 5)

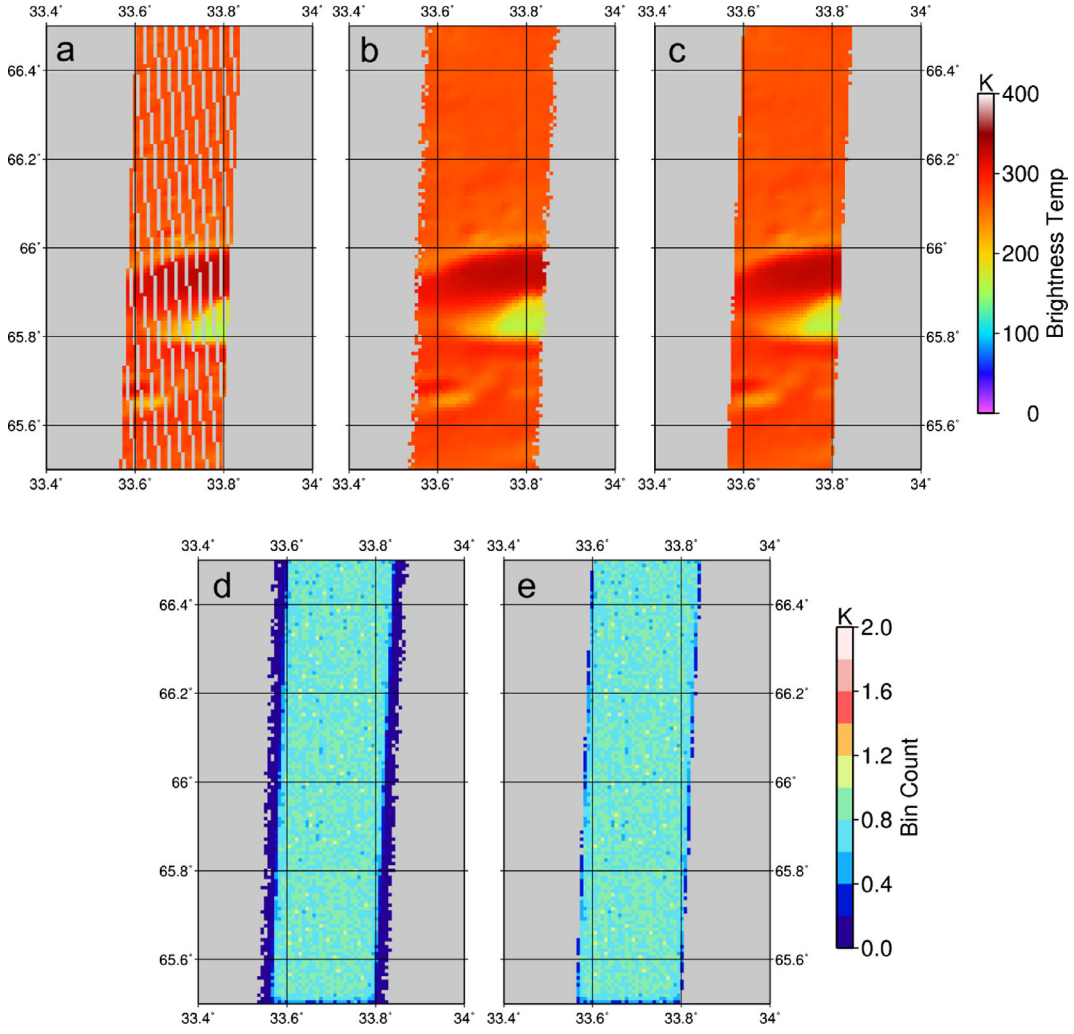

Fig. 4. (a) Diviner level 1 (RDR) data binned at 1/128° pix^{-1} resolution highlighting an individual swath of data from a single orbit. At high latitudes, the surface area of the individual bins become small relative to the surface footprint of the individual detectors and bins within the ground track are unpopulated during the binning process. (b) This aliasing is accounted for by populating bins with an additional $n = 100$ points using a two-dimensional probability distribution based on the detectors effective-FOV. (c) Sparsely populated bins at the edges of the ground track are eliminated by filtering the results with a bin count cutoff ensuring the width is preserved. (d and e) The bin counts corresponding to (b) and (c) normalized by n.

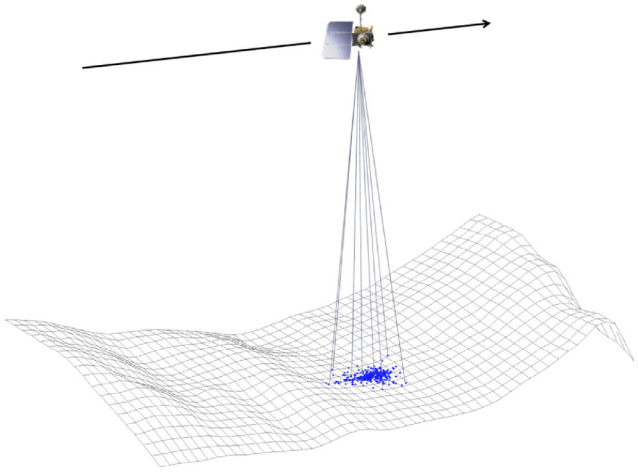

Fig. 5. Example Diviner EFOV from a single observation populated with points ($n = 100$) using the Monte Carlo method and ray traced onto a Lunar Orbiter Laser Altimeter DEM (Smith et al., 2010). Model points are assigned the same radiance value as the original observation and used as input into a binning routine (e.g. Sefton-Nash et al., 2015).

given the detector orientation relative to North (Fig. 6). The cloud of points will trend toward the actual EFOV as n increases, with the point density reflecting the probability distribution. Modeled points are assigned the same radiance value as the original observation and are used as input to a binning routine (e.g., Sefton-Nash et al., 2015). Assuming a sufficiently high point density within the point cloud, all bins that lie within the EFOV are therefore populated by the modeled point cloud. This eliminates the occurrence of empty bins, particularly at high latitudes in cylindrical projection where bin areas become small due to contraction in the longitude direction. Where adjacent detectors have overlapping EFOVs, points from different observations may reside in the same bins. The resulting radiance value of each bin is therefore the weighted mean of the observations that fall within it. The Diviner GDR (level 2) map products were processed in this manner using $n = 100$ points, which was sufficient to adequately resolve the EFOV while not being excessively CPU-intensive in the remaining processing pipeline.

The averaging of intersecting EFOVs that were acquired at different times is an acceptable representation of the lunar surface in this case, because subsequent observations are closely spaced in time (~0.128 ms). Caution should be exercised when binning ob-

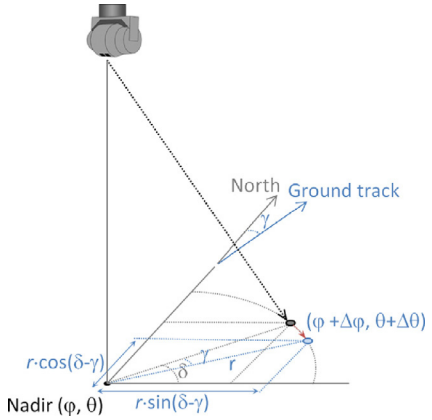

Fig. 6. Diviner in nadir viewing geometry with observation point at longitude, φ, and latitude, θ, and a modeled observation point at longitude, $\varphi + \Delta\varphi$, and latitude, $\theta + \Delta\theta$. Angle δ and distance r define the location of the model point on the surface in polar coordinates with the nadir observation at the origin and γ is the angle of rotation that aligns the point with the spacecraft ground track relative to north.

servations acquired at significantly different local times, because differences in illumination conditions between observations would cause gridded products to be less meaningful; they would average together multiple radiative states of the surface from different times of day.

Fig. 7 demonstrates the effectiveness of this processing step applied to data binned onto a grid in a polar stereo projection at 120 m pix^{-1} resolution. Diviner RDR (level 1) calibrated channel 8 (50–100 μm) radiance acquired between September 20, 2009 and October 17, 2009, as the Moon approached southern summer solstice, was binned and converted to brightness temperatures. The daytime only observations were acquired between 11.0 and 12.8 h of local time. This resolution results in aliasing because bins within individual orbit ground tracks are unpopulated (Fig. 7a). Applying the EFOV model during the binning process (Fig. 7b), this aliasing is eliminated without requiring any interpolation between bins.

4. Application: Brightness temperatures at Giordano Bruno crater

Giordano Bruno is a young Copernican-age crater with a diameter of 22 km near the eastern limb on the lunar far side (36°N, 103°E). The crater has a very fresh morphology with high rock abundance values derived from Diviner (Fig. 8) and an extensive ray system that is found to be extremely immature in spectral studies (Pieters et al., 1994; Lucey et al., 2000; Grier et al., 2001). The age of Giordano Bruno is estimated to be 1–10 Ma based on the crater size–frequency distribution of small craters superposed on its ejecta (Morota et al., 2009) and the morphologic prominence and size of distant secondaries near the Luna 24 landing site (Basilevsky and Head, 2012). It has been suggested that this age may be an overestimate as many of the craters superposed on the ejecta could be self-secondary craters (Plescia et al., 2010), craters formed by blocks of material ejected at high angles during the impact event that fall back onto the ejecta blanket (Shoemaker et al., 1969; Zanetti et al., 2015). This claim is bolstered by the observation of craters on the ejecta of Giordano Bruno containing impact melt deposits indicating a preexisting population of craters formed prior to emplacement of the impact melt demonstrating that at least some of the craters on the ejecta are self-secondary craters (Williams et al., 2014a).

The Diviner IR radiance measurements reveal a thermally heterogeneous and complex surface within and around Giordano Bruno. Fig. 9 shows brightness temperatures from a single orbit

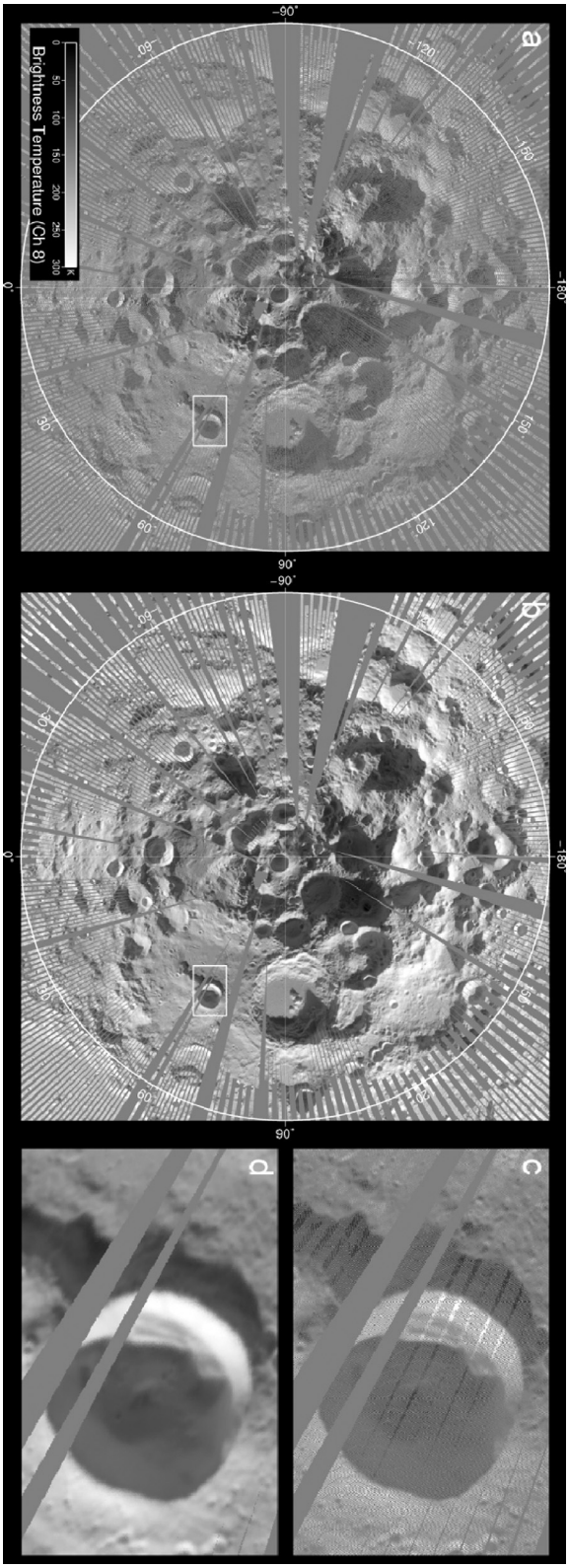

Fig. 7. (a) Brightness temperatures of the lunar south pole derived from Diviner channel 8 radiance acquired between September 20, 2009 and October 17, 2009 and binned in polar stereo projection at a resolution of 120 m pix^{-1}. (b) The same data binned with the addition of the modeled EFOV processing step applied. (c) Subframe of (a) and (d) subframe of (b) showing 28 km diameter crater Idel'son L at 84.2°S, 115.8°E.

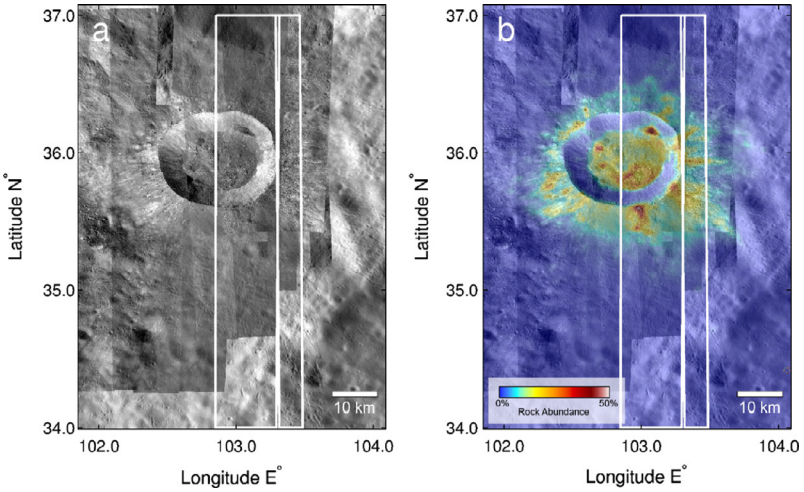

Fig. 8. (a) LROC NAC and WAC (Robinson et al., 2010) image mosaic of Giordano Bruno crater with (b) Diviner derived rock abundance superposed (Bandfield et al., 2011). White boxes show the Diviner ground tracks of LRO orbits 1479 (right) and 303 (left) shown in Fig. 9 and Fig. 11 respectively.

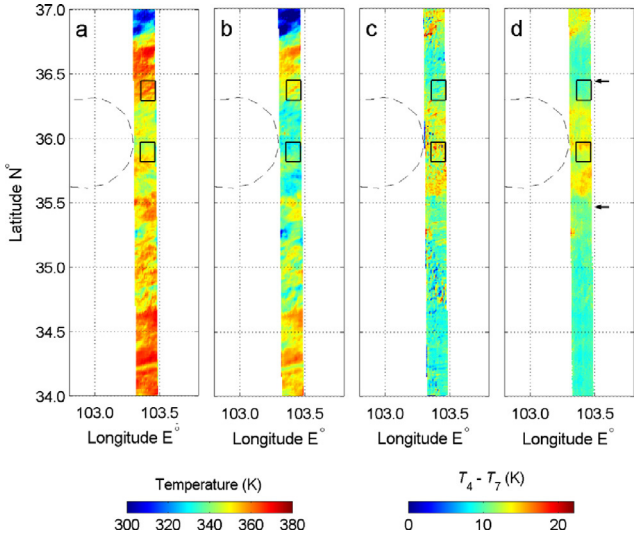

Fig. 9. Diviner data from LRO orbit 1479 acquired at an altitude of 57.33 km and binned at 1/128° pix^{-1}. (a) Diviner channel 4 brightness temperatures, (b) Diviner channel 7 brightness temperatures, (c) Diviner channels 4–7, and (d) Diviner channels 4–7 using the EFOV Monte Carlo modeling. By modeling the EFOV during the binning process, channels 4 and 7 become aligned and the speckling in the brightness temperature difference map in (c) is eliminated. The local time is 10.6 (late morning). Rocky areas are cooler in the morning as they warm slowly relative to areas free of blocky material. The mixture of temperatures in the FOV resulting from the rocks result in anisothermality in the Diviner channels as channel 4 is more sensitive to the warm temperatures and channel 7 the cooler temperatures within the FOV. The difference maps highlight how the anisothermality correlates with the blocky ejecta of Giordano Bruno. Dashed line outlines the crater rim. Black boxes show the location of LROC subframes in Fig. 10a (upper) and Fig. 10b (lower) and arrows show the latitude range used for the crater count densities in Fig. 13.

crossing the eastern flank of the crater from Diviner channels 4 and 7. The local time hour is 10.6 (late morning) revealing surface temperature differences as the terrain is heating up after the long lunar night. The lunar regolith is highly insulating and therefore responds rapidly to changes in illumination conditions relative to large rocks which have higher thermal inertias. This is evident in the brightness temperatures in Fig. 9 where the clastic, fine-grained ejecta is warmer than areas containing large fractions of rocks (Fig. 10).

Due to the non-linear nature of Planck radiance with respect to wavelength, the presence of surfaces radiating at different temperatures within Diviner's FOV will result in different brightness temperatures derived from the Diviner IR spectral bands (Bandfield et al., 2011; Williams et al., 2015). Measured brightness temperatures of an anisothermal surface will approach the weighted average of the temperatures within the FOV with increasing wavelength. Conversely, with decreasing wavelength, the measured brightness temperatures will approach the warmest temperatures within the FOV giving the shorter wavelength Diviner channels greater sensitivity to the warmer temperatures. In general, Diviner's FOV contains a mixture of temperatures due to small scale slopes, shadows, or rocks.

The distribution of small scale temperature gradients on the ejecta of Giordano Bruno result in higher brightness temperatures in Diviner's channel 4 (8.1–8.4 μm) (Fig. 9a) relative to channel 7 (25–41 μm) (Fig. 9b). The magnitude of this anisothermality can be quantified by differencing Diviner channels. However, there is a difference in the relative in-track positions of the field-of-view peaks for the Diviner channels. As a result there is spatial variation in which part of the surface is observed by the different channels during the 128 ms integration time for each detector observation. This leads to small misalignments between the channels and artifacts are introduced in maps when differencing channels because observations of two channels falling in a given map pixel may not represent radiance from the identical location on the lunar surface (Fig. 9c). By modeling each observation's EFOV, the spatial contributions from the lunar surface for each channel are reconciled. Artifacts are significantly reduced, allowing meaningful comparisons to be made between channels to determine the magnitude of anisothermality (Fig. 9d). This enables quantitative assessment of the abundance of high thermal inertia material, such as boulders in ejecta blankets. Differencing channels (T_4–T_7) reveals the heterogeneity in the thermophysical properties of the material near the rim of Giordano Bruno. The regions containing numerous large blocks display higher T_4–T_7 values as the blocks remain cooler than the surrounding material in the AM hours. The mixture of cooler rocks and warmer clastic ejecta, results in greater anisothermality.

At higher orbital altitudes and/or elliptical orbits, the aliasing in the gridded data becomes more severe. Fig. 11 shows bolometric brightness temperatures derived from all 7 IR Diviner channels (Paige et al., 2010b) for LRO orbit 303 during the commissioning mission phase when the spacecraft was in an elliptical orbit. The spacecraft altitude was 161.7 km when this data was acquired, about three times the altitude when in its near-circular orbit during the nominal mapping phase of the mission. The data is binned at 1/128° pix^{-1} as it was in Fig. 9; however the ground track is now

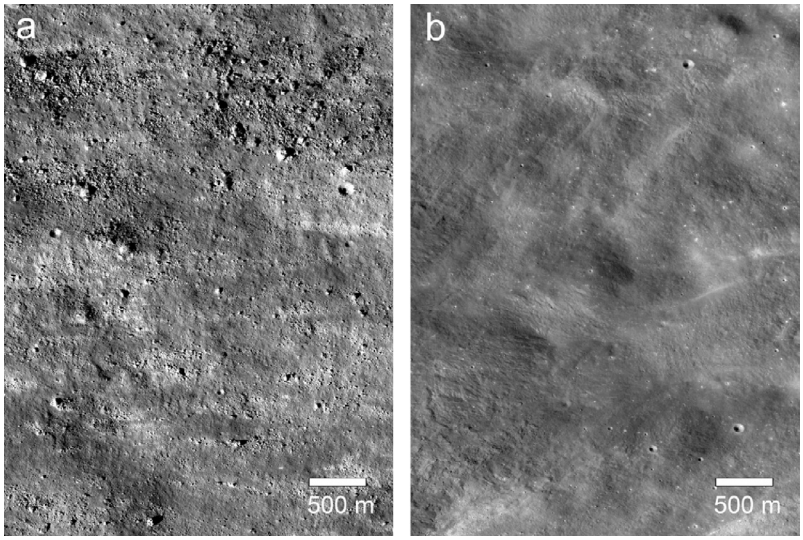

Fig. 10. Portions of LROC NAC image M182860930R (NASA/GSFC/Arizona State University). (a) Area of cooler morning temperatures and elevated anisothermality between Diviner channels 4 and 7. (b) Area of relatively lower anisothermality and warmer morning temperatures.

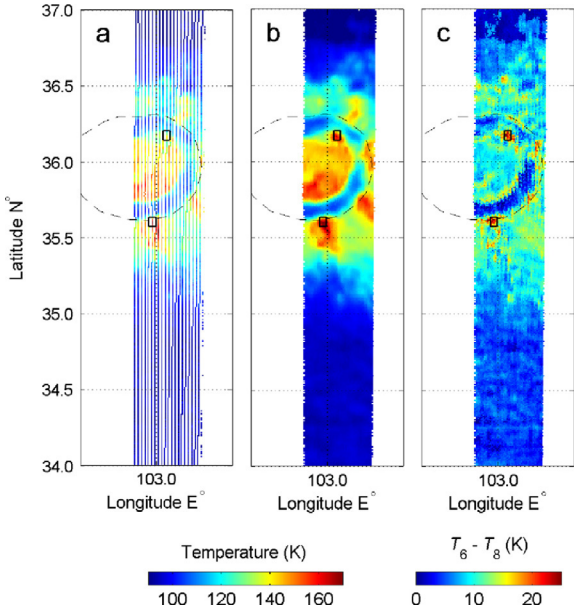

Fig. 11. Diviner nighttime data (local time hour 4.9) binned at 1/128° pix^{-1} from LRO orbit 303 acquired at an altitude of 161.73 km during the commissioning mission phase when LRO was in an elliptical orbit. (a) Diviner bolometric brightness temperatures derived from all 7 IR channels without EFOV model and (b) with EFOV model. The higher spacecraft altitude results in individual detectors having wider ground projected EFOV causing greater separation between populated bins when the EFOV is not accounted for during the binning process. (c) Diviner channels 6–8 showing anisothermality in nighttime temperatures. The dashed curve shows the location of the crater rim. Black boxes show the locations of LROC subframes Fig. 12a (lower) and Fig. 12b (upper) centered on the bins with the highest anisothermality.

wide enough that gaps appear in the gridded data. Applying our EFOV model, these gaps are populated with data as these regions were within the instrument's FOV and contributed to the measurements (Fig. 11b).

This data was acquired at a local time hour of 4.9, prior to sunrise in the early morning when lunar temperatures are near their lowest. The warmest temperature in Fig. 11b is 170.9 K, compared with the typical nighttime temperatures at the equator which are ~100 K in the am hours (Vasavada et al., 2012). The regolith absorbs sensible heat during the daytime and radiates the heat back to space during the long lunar night. Rocks, having a higher thermal inertia, act as reservoirs of heat during the nighttime. The regolith cools rapidly after sunset while the rocks remain warmer though the night resulting in anisothermality in Diviner nighttime observations. Differencing Diviner channels 6 and 8 (T_6–T_8) reveals areas where large rocks have remained warm through the lunar night (Fig. 11c). The greatest anisothermality between the two channels occurs in two areas with a high density of large rocks observed in LROC NAC images (Fig. 12).

The anisothermality observed around Giordano Bruno shows that the crater and its ejecta exhibit substantial heterogeneity in thermophysical properties. The rockiness responsible for the large variations in brightness temperatures in both the daytime and nighttime observations, and the large blocks of material observed in LROC NAC images, are consistent with a recent, <10 Ma, formation age as the breakdown of rocks and the accumulation of regolith on the Moon is fairly rapid (Ghent et al., 2014).

Such heterogeneity of materials also has implication for crater counts around Giordano Bruno as different impact target materials can influence crater size–frequency distributions, and thus derived absolute model ages. For example Dundas et al. (2010) and van der Bogert et al. (2015) have demonstrated how variation in impact crater scaling from differing target properties can be significant enough to influence geologic interpretations. Crater counts conducted along a portion of the LRO orbit 1479 ground track (Fig. 9) shows a reduction in the density of craters where T_4–T_7 anisothermality is higher (Fig. 13). The large blocks that characterize the regions with high T_4–T_7 values possibly inhibit crater formation as the energy and momentum of impactors is expended on fragmenting and pulverizing the blocks rather than forming a crater, a possible explanation considered for the observed depletion of small craters on the asteroid Eros (Chapman et al., 2002). This could in part explain the discrepancies in crater count size–frequency distributions (SFDs) observed on Giordano Bruno's ejecta (Plescia et al., 2010; Williams et al., 2014a). Plescia et al. (2010) interpret variations in the slope and magnitude they observe in the crater SFDs to indicate the crater population is predominately comprised of self-secondary craters rather than a population of primary craters which should have a more consistent, and predictable SFD (e.g. Ivanov, 2006; Williams et al., 2014b). This would imply the true age of the Giordano Bruno is younger than a model age derived from these craters. However, if the large blocks on the ejecta are

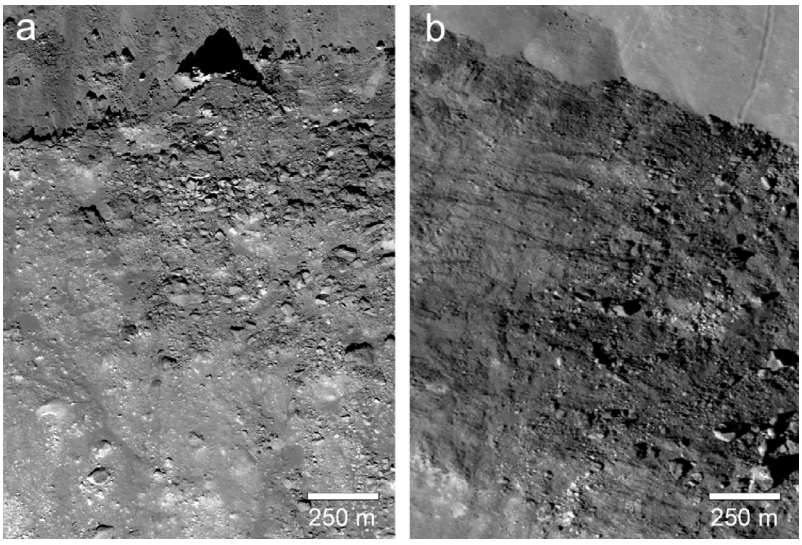

Fig. 12. Two locations within the orbit 303 ground track with the greatest anisothermality in nighttime temperatures: (a) T_6–$T_8 = 26.56$ K near the south rim and (b) T_6–$T_8 = 28.48$ K on a bench within the interior northeast wall. Portion of LROC NAC image pair (a) M108555806 and image (b) M1098165325R (NASA/GSFC/Arizona State University).

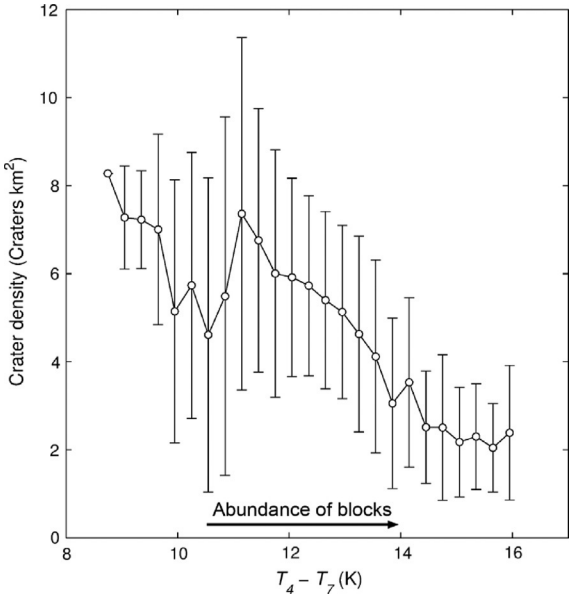

Fig. 13. The number density of craters on the ejecta of the eastern margin of Giordano Bruno decreases where T_4–T_7 anisothermality in LRO orbit 1479 (Fig. 9) is higher.

suppressing crater formation, this would have the inverse effect on model ages resulting in an under prediction of the true formation age of Giordano Bruno as some primary impact events would not result in craters. This indicates that craters with diameters of similar or smaller length scale to blocks on the surface (<100 m in this case) should be used with caution.

5. Conclusions

We present a method to improve accuracy and address issues associated with binning point-based datasets. Using knowledge of instrumental characteristics and spacecraft and observation geometry, we model the effective, ground projected field-of-view for each observation prior to binning that data. The EFOV is discretized into individual points using a Monte Carlo approach. Subsequent binning with these points then provides binned data with measured values given the correct surface area representation with the appropriate weight in each bin. This approach has the benefit of ensuring all bins are populated that was within a detectors field-of-view when a measurement was acquired, with correct weighting of all the cumulative values in a bin. Further, the location on the surface with the highest probability of contributing to a measurement can be identified, and may not be the same as predicted by the IFOV of the detector due to in-track smearing. For multispectral data, this approach can improve the alignment of different spectral channels in the gridding process and reduce errors.

This processing is applied to Diviner data acquired at the Copernican-age crater Giordano Bruno. Brightness temperature data reveal this area to exhibit significant variations in thermophysical properties. Regions of elevated anisothermality in mid-morning daytime and early morning nighttime temperatures correlate with areas containing large rocks observed in LROC NAC images. Such heterogeneity in the ejecta material has implications for modeled crater count age-dates as impact crater formation appears to be suppressed in areas displaying higher anisothermality. This indicates that for surfaces with numerous blocks, crater SFDs at diameters comparable or smaller than the block sizes, are likely unreliable and will produce younger model ages. Crater counts conducted over a large portion of the ejecta yield a model age 1–10 Ma (Morota et al., 2009). The heterogeneous thermal characteristics of the crater and its ejecta, along with its fresh appearance and the presence of large blocks, are consistent with this very young formation age.

Acknowledgments

We would like to thank Karin Bauch and an anonymous reviewer for their helpful comments and the LRO, LROC, LOLA, and Diviner operations teams for the collection of high quality datasets used in this work. Support for this work was provided by the Lunar Reconnaissance Orbiter program.

References

Bandfield, J.L., et al., 2011. Lunar surface rock abundance and regolith fines temperatures derived from LRO Diviner Radiometer data. J. Geophys. Res. 116, E00H02. doi:10.1029/2011JE003866.

Bandfield, J.L., et al., 2015. Lunar surface roughness derived from LRO Diviner Radiometer observations. Icarus 248, 357–372.
Basilevsky, A.T., Head, J.W., 2012. Age of Giordano Bruno crater as deduced from the morphology of its secondaries at the Luna 24 landing site. Planet. Space Sci. 73, 302–309.
Chapman, C.R., et al., 2002. Impact history of eros: Craters and boulders. Icarus 155, 104–118.
Chin, G., et al., 2007. Lunar Reconnaissance Orbiter overview: The instrument suite and mission. Space Sci. Rev. 129, 391–419. doi:10.1007/s11214-007-9153-y.
Dundas, C.M., et al., 2010. Role of material properties in the cratering record of young platy-ridged lava on Mars. Geophys. Res. Lett. 37, L12203. doi:10.1029/2010GL042869.
Ghent, R.R., et al., 2014. Constraints on the recent rate of lunar ejecta breakdown and implications for crater ages. Geology 42, 1059–1062.
Glotch, T.D., et al., 2010. Highly silicic compositions on the Moon. Science 329, 1510. doi:10.1126/science.1192148.
Glotch, T.D., et al., 2011. The Mairan domes: Silicic volcanic constructs on the Moon. Geophys. Res. Lett. 38, L21204. doi:10.1029/2011GL049548.
Greenhagen, B.T., et al., 2010. Global silicate mineralogy of the Moon from the Diviner Lunar Radiometer. Science 329, 1507. doi:10.1126/science.1192196.
Grier, J.A., et al., 2001. Optical maturity of ejecta from large rayed lunar craters. J. Geophys. Res. 106, 32847–32862.
Ivanov, B.A., 2006. Earth/Moon impact rate comparison: Searching constraints for lunar secondary/primary cratering proportion. Icarus 183, 504–507.
Lucey, P.G., et al., 2000. Imaging of lunar surface maturity. J. Geophys. Res. 105, 20377–20386.
Morota, T., et al., 2009. Formation age of the lunar crater Giordano Bruno. Meteorit. Planet. Sci. 44, 1115–1120.
Paige, D.A., et al., 2010. The Lunar Reconnaissance Orbiter Diviner Lunar Radiometer Experiment. Space Sci. Rev. 150, 125–160. doi:10.1007/s11214-009-9529-2.
Paige, D.A., et al., 2010. Diviner Lunar Radiometer observations of cold traps in the Moon's south polar region. Science 330, 479–482. doi:10.1126/science.1187726.
Paige, D.A. et al., 2011. LRO Diviner Lunar Radiometer global mapping results and gridded data product. Lunar Planet. Sci. 42. Abstract 2544.
Pieters, C.M., et al., 1994. A sharper view of impact craters from clementine data. Science 266, 1844–1848.
Plescia, J.B., Robinson, M.S., Paige, D.A., 2010. Giordano Bruno: The young and the restless. Lunar Planet. Sci. 41. Abstract 2038.
Robinson, M.S., et al., 2010. Lunar Reconnaissance Orbiter Camera (LROC) instrument overview. Space Sci. Rev. 150, 81–124. doi:10.1007/s11214-010-9634-2.
Sefton-Nash, E., et al., 2015. Diviner Lunar Radiometer gridded brightness temperatures from geodesic binning of modeled fields of view. Icarus (submitted for publication).
Shoemaker, E.M. et al., 1969. Television observations from surveyor. In: Surveyor Program Results NASA SP-184, pp. 19–128.
Smith, D.E., et al., 2010. The Lunar Orbiter Laser Altimeter investigation on the Lunar Reconnaissance Orbiter mission. Space Sci. Rev. 150, 209–241.
Song, E., et al., 2013. Bulk mineralogy of lunar crater central peaks via thermal infrared spectra from the Diviner Lunar Radiometer: A study of the Moon's crustal composition at depth. J. Geophys. Res. 118, 689–707. doi:10.1002/jgre.20065.
Sullivan, M.T. et al., 2013. Lunar Reconnaissance Orbiter Diviner Lunar Radiometer Experiment: Reduced Data Record and Derived Products Software Interface Specification. Tech. Rep. Version 1.13, PDS Geosciences Node.
Tooley, C.R., et al., 2010. Lunar Reconnaissance Orbiter mission and spacecraft design. Space Sci. Rev. 150, 23–62. doi:10.1007/s11214-009-9624-4.
van der Bogert, C.H., et al., 2015. Origin of discrepancies between crater size–frequency distributions of coeval lunar geologic units via target property contrasts. Icarus (submitted for publication).
Vasavada, A.R., et al., 2012. Lunar equatorial surface temperatures and regolith properties from the Diviner Lunar Radiometer Experiment. J. Geophys. Res. 117, E00H18. doi:10.1029/2011JE003987.
Vondrak, R., et al., 2010. Lunar Reconnaissance Orbiter (LRO): Observations for lunar exploration and science. Space Sci. Rev. 150, 7–22.
Williams, J.-P. et al., 2014a. Crater size–frequency distribution on the ejecta of Giordano Bruno. Lunar Planet. Sci. 45. Abstract 2882.
Williams, J.-P., Pathare, A.V., Aharonson, O., 2014. The production of small primary craters on Mars and the Moon. Icarus 235, 23–36.
Williams, J.-P., et al., 2015. The global surface temperatures of the Moon as measured by the Diviner Lunar Radiometer Experiment. Icarus (submitted for publication).
Zanetti, M., et al., 2015. Evidence for auto-secondary cratering of Copernican complex crater ejecta blankets. Icarus (submitted for publication).